Diurnal variations of the Fe layer in the mesosphere and lower thermosphere: Four season variability and solar effects on the layer bottomside at McMurdo (77.8°S, 166.7°E), Antarctica

Zhibin Yu,[1] Xinzhao Chu,[1] Wentao Huang,[1] Weichun Fong,[1] and Brendan R. Roberts[1]

Received 8 May 2012; revised 25 September 2012; accepted 1 October 2012; published 21 November 2012.

[1] We provide one of the first reports on diurnal variations of the Fe layer in the mesosphere and lower thermosphere (MLT) using nearly 1000 h of data collected with an Fe Boltzmann lidar at McMurdo, Antarctica from December 2010 through 2011. The Fe layer undergoes significant diurnal variations on the bottomside in autumn and spring with daytime downward extension and nighttime upward contraction. Such variations are absent in winter under 24-h darkness. Summertime Fe density perturbations exhibit downward tidal phase progression. The bottom growth/contraction of Fe layer is shown to be a solar effect that is closely correlated with the solar elevation angle. The bottom transition corresponds to the solar elevation between −9° and −1° when sunlight passes through the lower atmosphere before reaching the MLT. Once the solar elevation is above −1°, the layer bottom remains nearly flat at its daytime altitude (∼70–73 km). When the solar elevation is below −9°, the layer bottom stays at its nighttime altitude (∼78–80 km). The descending transition rate at dawn is faster than the ascending rate at dusk. The time delay between appreciable Fe density and sunrise/sunset at the MLT increases with decreasing altitude and varies with season. We describe qualitatively how both neutral Fe chemistry with H, O and O_3 and photolysis of Fe-containing molecular species may play important roles in Fe diurnal variations. Accurate rate coefficients for Fe neutral and photochemical reactions are essential to quantitatively explain the solar effects in diurnal variations of the Fe layer.

Citation: Yu, Z., X. Chu, W. Huang, W. Fong, and B. R. Roberts (2012), Diurnal variations of the Fe layer in the mesosphere and lower thermosphere: Four season variability and solar effects on the layer bottomside at McMurdo (77.8°S, 166.7°E), Antarctica, *J. Geophys. Res.*, *117*, D22303, doi:10.1029/2012JD018079.

1. Introduction

[2] Iron (Fe) and sodium (Na) are the two most abundant gas-phase metal species in the mesosphere and lower thermosphere (MLT) [*Plane*, 2003]. Both Fe and Na atoms have been used by lidars as excellent tracers in the MLT to infer temperature and wind, and thereby thermal structures, dynamics, chemistry and neutral-ion coupling (see summary by *Chu and Papen* [2005]). The existence of meteoric metal layers was discovered by analyzing the spectra of atmospheric nightglow or twilight emissions [*Slipher*, 1929; *Hunten*, 1967; *Broadfoot and Johanson*, 1976], and later confirmed by resonance fluorescence lidar measurements [e.g., *Bowman et al.*, 1969; *Granier et al.*, 1985, 1989]. Fe and Na layers share many common features, e.g., both come from meteoric ablation and exhibit similar seasonal variations with summer low and autumn/winter high column abundances [*Kane and Gardner*, 1993a; *Gardner et al.*, 2005; *Yi et al.*, 2009; *Gerding et al.*, 2000]. Nevertheless, the new lidar observations to be reported in this study reveal a significant extension downward of the Fe layer bottomside when the Sun rises and contraction when the Sun sets. Such behavior is not observed in Na [*Clemesha et al.*, 1982; *States and Gardner*, 1999; *Plane*, 2004]. These new data indicate the importance of photochemistry in the metal layers, and the different responses of Fe and Na layers to solar illumination variations challenge the current understanding of metal chemistry in the upper atmosphere.

[3] Unlike the extensive studies of Na layers by lidars, there have not been any reports in the literature on either the diurnal variations of or the solar effects on the Fe layer (except the photo-ionization of Fe atoms) until this study. Fe lidar observations have been made at low latitudes at Arecibo (18°N) [*Raizada and Tepley*, 2003; *Zhou et al.*, 2008], midlatitudes at Urbana (40°N), Kühlungsborn (54°N) and Wuhan (30°N) [*Kane and Gardner*, 1993a,b; *Gerding et al.*, 2000; *Yi et al.*, 2009; *Ma and Yi*, 2010], and high

[1]Cooperative Institute for Research in Environmental Sciences and Department of Aerospace Engineering Sciences, University of Colorado Boulder, Boulder, Colorado, USA.

Corresponding author: X. Chu, Cooperative Institute for Research in Environmental Sciences, University of Colorado Boulder, 216 UCB, Boulder, CO 80309, USA. (xinzhao.chu@colorado.edu)

0148-0227/12/2012JD018079

latitudes at Andoya (69°N), the North Pole (90°N), the South Pole (90°S), Rothera (67.5°S) and McMurdo (77.8°S) [*Alpers et al.*, 1990, 1994; *Gardner et al.*, 2001; *Gardner et al.*, 2005, 2011; *Chu et al.*, 2011a, 2011b]. However, these reports mainly focus on the seasonal and latitudinal variations, sporadic layers, meteor trails, thermospheric Fe layers and waves [*Chu et al.*, 2011b], and polar summer events in connection with polar mesospheric clouds (PMCs) and space shuttle plumes [*Plane et al.*, 2004; *Stevens et al.*, 2005]. Because most observations made at mid to low latitudes were nighttime only, they could not reveal the diurnal variations. Although observations made at the South Pole and Rothera, Antarctica covered full diurnal cycles, there was very little coverage during the transition time of solar illumination in the autumn and spring, obscuring the study of solar effects on the Fe layer. The new observations reported in this paper covered full diurnal cycles in all four seasons at McMurdo (77.83°S, 166.67°E). In particular, continuous lidar observations were made in the autumn and spring during the transition of solar illumination between daylight and night darkness, enabling studies of solar effects in the diurnal variations of the Fe layer.

[4] Knowledge of Fe layer characteristics in the MLT has been dramatically improved in the last two decades, owing to lidar observations by numerous groups as mentioned above, and the modeling and laboratory work by Plane and coworkers [e.g., *Helmer et al.*, 1998; *Self and Plane*, 2003; *Plane et al.*, 2003]. A coupled chemical and dynamical system determines the characteristics and variations of neutral Fe layers and Fe-containing species in the MLT. For the sake of later discussion, we summarize the current understanding here based on a recent work by *Gardner et al.* [2011]. The source of Fe and Fe species in the MLT is meteoric ablation. Sporadic meteoroids are the major sources, although meteor showers also contribute [*Plane*, 2004; *Ceplecha et al.*, 1998; *Baggaley*, 2002]. Several tens of tons of micrometeors are believed to enter the Earth's atmosphere every day [*Plane*, 2004]. The meteor influx is balanced by the downward transport to chemical sinks below 85 km. The residence time for a typical Fe atom in the layer is several days before it is removed to a stable reservoir. FeOH is believed to be the major reservoir species for Fe [*Plane et al.*, 2003]. FeOH and other Fe-containing molecules are then permanently removed from the MLT region by forming or condensing onto meteor smoke particles that eventually settle into the stratosphere under the influence of gravity [*Saunders and Plane*, 2006]. Therefore, the Fe system is not a closed system cycling among neutral Fe atoms, Fe^+ ions and Fe-containing species, but an open system with meteor input at high altitudes as the sources, and permanent removal on meteor smoke particles below the mesopause as the sinks. Such Fe-rich meteor smoke particles are transported downward through the stratosphere and troposphere and eventually settle onto the Earth's surface.

[5] The partitioning among Fe, Fe^+ and Fe-containing species is altitude dependent. On the topside of the Fe layer, ion chemistry predominates, while neutral chemistry dominates the underside [*Self and Plane*, 2002; *Plane*, 2003]. Most of the important chemical reactions have been studied in the laboratory, and their reaction rate coefficients and temperature dependence have been measured [e.g., *Plane et al.*, 2003; *Vondrak et al.*, 2006; *Woodcock et al.*, 2006]. In ion-molecule chemistry, neutral Fe atoms are converted to Fe^+ mainly via charge transfer with NO^+ and O_2^+, but photoionization of Fe also contributes. The conversion back to neutral Fe is mainly through dissociative electron recombination after various ion compounds are formed, as the direct recombination of Fe^+ with electrons is a slow process. The neutral Fe chemistry at the underside of the Fe layer is mainly controlled by odd oxygen (O and O_3) and hydrogen (H) chemistry, although reactions with H_2O, CO_2 and O_2 are also important. Consequently, the underside of the Fe layer is highly sensitive to O, H and O_3 concentrations. Fe chemistry is quite temperature dependent, as the reaction of FeOH with H has a significant activation energy, causing the partitioning of iron between Fe and FeOH to shift to the former at higher temperatures [*Plane*, 2003; *Gardner et al.*, 2011]. Besides the above factors (ablation, transport, removal, partitioning with ion-molecule and neutral chemistry, O, H and O_3 concentrations, and temperatures), two more factors should be added to the study of the diurnal variations of Fe layers: One is the influence of atmospheric tides and another is Fe photochemistry, analogous to the study of Na diurnal variations [*Plane*, 2004]. For high polar latitudes, geomagnetic activity and particle precipitation influence the ion and electron densities in the ionosphere, potentially affecting ion-molecule chemistry. In addition, Fe depletion via heterogeneous removal by mesospheric ice particles is a big effect in summer at high polar latitudes [*Plane et al.*, 2004; *Gardner et al.*, 2011].

[6] Many uncertainties and unknowns remain in these factors and their effects on the Fe layer and its diurnal variations. In particular, none of the photochemical reactions of Fe-containing molecular species has been included in the currently published Fe chemistry models. Therefore, the diurnal variations of the Fe layer are a new region to explore, with the solar effects on the Fe layer far from being understood. This paper provides one of the first observational reports of Fe diurnal variations and solar effects on the Fe layer bottomside using Fe Boltzmann lidar measurements made at McMurdo, Antarctica from December 2010 through the end of 2011, along with an individual case in March 2012. The nearly 1000 h of data allow the characterization of Fe diurnal variations in four seasons throughout the year as well as more in-depth case studies. Quantitative information is derived from the lidar data for comparison with future Fe modeling. A most significant feature of the reported measurements is the distinct bottomside extension of the Fe layer during local sunrise and contraction during sunset. We argue that daytime Fe production below 80 km is related to photochemistry involving the Fe-containing species and neutral Fe chemistry with H, O and O_3. These entirely new results provide direct, real-time quantitative evidence for the influence of solar UV radiation on the chemistry and composition of the mesopause region.

2. McMurdo Lidar Campaign and Data Analysis

[7] To fill a critical data gap in observations of the mesospheric metal layers between the South Pole and the Antarctic Circle, the University of Colorado lidar group deployed an Fe Boltzmann lidar to McMurdo Station (77.83°S, 166.67°E) and has been collecting data since the austral summer of 2010–2011 [*Chu et al.*, 2011a, 2011b]. McMurdo is located on Ross Island, and this lidar campaign is a collaboration between the United States Antarctic Program (USAP) and

Table 1. Lidar Observations of Fe Layers at McMurdo From December 2010 Through 2011[a]

Month	Jan	Feb	Mar	Apr	May	Jun	Jul	Aug	Sep	Oct	Nov	Dec	Total
Days	8	7	8	4	6	4	3	5	1	3	9	8	66
Hours	173	108	47	54	59	70	48	72	9	55	122	146	963

[a]December data were taken in both 2010 and 2011, while the other months were in 2011 only. The 20-h of data on 20–21 March 2012 used for case studies were not included in this table.

Antarctica New Zealand (AntNZ). The lidar was successfully installed in the AntNZ facility at Arrival Heights near McMurdo, and the first Fe signals were obtained on 16 December 2010. Since then, the University of Colorado lidar researchers have operated the lidar around the clock, weather permitting, through all 12 months of the year to acquire as many Fe observations as possible. Developed at the University of Illinois more than a decade ago [e.g., *Chu et al.*, 2002], the lidar system consists of two independent channels operating at two neutral Fe absorption lines, 372 nm and 374 nm, respectively. Thus, the lidar measures the Fe layers in two different wavelengths, and the ratio between these two channels is used to derive temperatures in the MLT region [*Gelbwachs*, 1994; *Chu et al.*, 2002]. Owing to the narrowband interference filters and Fabry-Perot etalons employed in the lidar receivers and the high-power pulsed alexandrite lasers employed in the lidar transmitters, this Fe Boltzmann lidar is capable of full-diurnal measurements of Fe density and temperature, along with Rayleigh temperature in the altitude range of ~30 to 70 km. Principles, capabilities and error analysis of the lidar can be found in [*Chu et al.*, 2002]. Before its deployment to McMurdo, this Fe Boltzmann lidar was refurbished and upgraded at the University of Colorado to restore its specifications and to further enhance its spectral stability, temporal resolution and daytime capability [*Chu et al.*, 2011a; *Wang et al.*, 2012]. Such full-diurnal capabilities enable our investigation of the diurnal variations of the MLT Fe layer in the current study.

[8] In Table 1 we summarize the distribution of lidar observations from 16 December 2010 through the end of 2011, which are used in the current study. The 20 h of data taken on 20–21 March 2012 were also used in the case study but not included in the table. More data were collected during the four summer months (November through February) than in the other three seasons because of greater availability of lidar personnel and better weather conditions. From March through August weather conditions limited the data collection, although a single operator each year (Z. Yu in 2011 and B. Roberts in 2012) would try his best to establish more than 24-h continuous observations. In September and October 2011, the campaign suffered temporary instrument difficulties, resulting in low data coverage. As a consequence, the current data set is adequate for seasonal studies of diurnal variations, but not for monthly studies. The diurnal distributions of data hours plotted in Figure 1 demonstrate the availability of sufficient data samples for all four seasons. Here the definition of season is based on the solar illumination conditions in the MLT region. Polar summer experiences 24-h sunlight and polar winter is under 24-h darkness, while the polar autumn and spring have alternation of day and night. The seasonal divisions and the observation hours in each season are given in Table 2. We defined the seasons this way to assess the diurnal impacts of solar illumination on the Fe layers, which is greatest in autumn and spring.

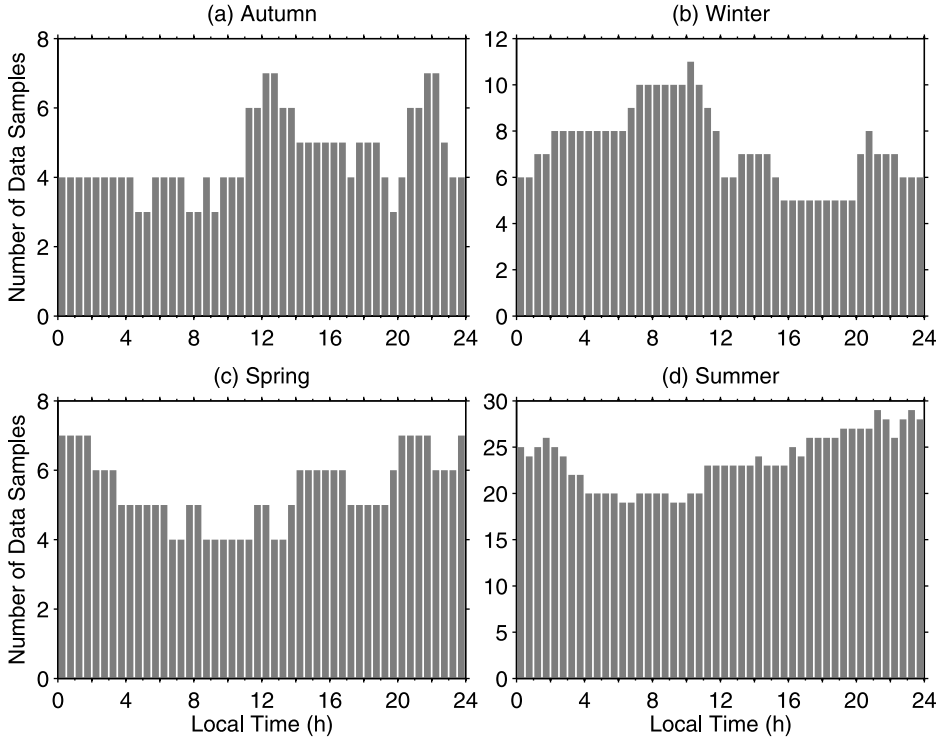

Figure 1. Diurnal distribution of half-hourly lidar data samples in the season of (a) autumn, (b) winter, (c) spring, and (d) summer.

Table 2. Southern Polar Season Division and Total Observational Hours

Season	Start Date to End Date	Total Observational Hours
Polar Autumn	1 Mar 2011 to 6 May 2011	112 h
Polar Winter	7 May 2011 to 6 Aug 2011	175 h
Polar Spring	7 Aug 2011 to 31 Oct 2011	127 h
Polar Summer	1 Nov 2011 to 28 Feb 2011	549 h

[9] The first step in analyzing the data is to form a composite day of Fe density profiles for each season by adding together all the data taken during the same season at a particular time and altitude. Outliers caused by sporadic Fe layers were removed with a box plot method [*Tukey*, 1977] before taking arithmetic means for each seasonal composite. The data resolutions are set to a fixed 100 m × 0.5 h grid in order to quantify the Fe layer consistently through the year. The data in every half hour starting with 0 or 0.5 h are grouped to represent the half hour grid. The final composite contours are smoothed by a 2-D Hanning window with 1-km spatial and 2-h temporal full-width-at-half-maximum (FWHM). By taking composite means, the effects of noncoherent waves are reduced, helping reveal the true diurnal variations.

3. Diurnal Variations of the Fe Layer Through Four Seasons

[10] Four seasonal composites of diurnal variations of Fe densities are plotted versus local time and altitude in Figures 2a–2d for autumn, winter, spring and summer. Summer Fe layers show lower density, higher altitude, and narrower width than those of the other three seasons. The winter topside extends to over 105 km, much higher than the other seasons. The peak of Fe density occurs around 86–87, 85–86, ~84 and 90 km for autumn, winter, spring, and summer. Around the peak, Fe density undergoes substantial variations through a diurnal cycle in each season with a tendency of higher peak density around local noon and lower density near local midnight. A striking feature in the seasonal composites is the downward extension of the Fe layer on the bottomside during the day in autumn and spring. In Figures 2a and 2c, the layer bottom changes from ~80 km in the night to ~72 km around noon. Interestingly, the downward extension in the morning has a steeper slope than the upward contraction in the afternoon.

[11] The density perturbations are plotted in Figures 2e–2h, which are derived by taking the differences between the half-hourly mean Fe profiles and the diurnal-mean Fe density profile at each altitude in the corresponding season. Around and below 80 km in the autumn and spring (Figures 2e and 2g), Fe density enhancement during the day and reduction in the night result from the layer bottom extension observed in Figures 2a and 2c. However, the winter density perturbations at the bottom in Figure 2f appear to be random with local time when sunlight is absent from the MLT. These phenomena indicate that the daytime downward extension on the bottomside is a solar effect, which is strongly influenced by the diurnal variation of solar illumination. In Figure 2h, the summer density perturbations show a weak enhancement near 84 km around noon. This is likely related to the tides observed in the main layer, and the Fe layer around this altitude is also strongly influenced by PMC ice particles in the polar summer.

[12] In the summer main layer between 84 and 98 km, the Fe density perturbations (Figure 2h) clearly show a downward phase progression with the vertical phase speed of about −1.25 km/h. The 24- and 12-h oscillations have comparable amplitudes. Such clear phase progressions likely represent tidal perturbations in the summer. This is because averaging over 20–25 data samples (Figure 1) in each time bin largely reduces the perturbations caused by gravity waves, helping reveal the tidal perturbations. Strong wave perturbations with amplitudes as large as 20–30 K have been found in the lidar temperatures at McMurdo [*Chen et al.*, 2012; *Chu et al.*, 2011a, 2011b, 2012], but the tidal amplitudes are only ~2–4 K in the winter according to our preliminary results. The complex structures in autumn, winter and spring main layers are most likely due to residual gravity wave effects because the data samples in these seasons number only 4–5 for most hours of the day. We notice that the tidal perturbations in the summer Fe layer at McMurdo are comparable to the tidal features observed by a lidar at Davis (69°S, 78°E), Antarctica in the summer season of 2010–2011 [*Lübken et al.*, 2011].

[13] To further characterize the diurnal variations of Fe layers in the four seasons, the Fe column abundances, centroid altitudes, RMS widths, and bottom altitudes are derived from the seasonal composites of Fe densities, and the results are plotted in Figure 3. The integration range for the first three parameters is from 70 to 105 km, and the bottom altitude is defined as the altitude of the 300-cm^{-3} Fe density contour on the bottomside. The summer layers are quite distinct from the other three seasons with lower abundance and smaller width but higher centroid and bottom altitudes. This is consistent with the current understanding that both the low MLT temperature in the polar summer and the heterogeneous removal of Fe atoms by visible and sub-visible ice particles significantly reduce the Fe density, especially below ~90 km thus making the surviving layers weaker, narrower and weighted to higher altitude [*Plane et al.*, 2004; *Gardner et al.*, 2005, 2011]. In addition, the upwelling over the summer pole associated with the summer-to-winter-pole meridional circulation also contributes to the higher layer altitudes via advective transport [*Gardner et al.*, 2005]. To characterize the dominant harmonic components, a harmonic fit consisting of mean plus diurnal, semidiurnal and terdiurnal oscillations, as per equation (1), is applied to the Fe parameters for all four seasons:

$$y = A_0 + A_{24}\cos\left[\frac{2\pi}{24}(t - P_{24})\right] + A_{12}\cos\left[\frac{2\pi}{12}(t - P_{12})\right] + A_8\cos\left[\frac{2\pi}{8}(t - P_8)\right]. \quad (1)$$

The fitting results are shown as the solid curves in Figure 3, and the fitted parameters are summarized in Table 3. The large correlation coefficients in most of the fits indicate good correlations between the fitting equation and the data.

[14] Both the centroid and bottom altitudes in autumn and spring show strong dependence on local time with noon altitudes lower than those in the night. The amplitudes of the fitted diurnal oscillations are much larger than those of the

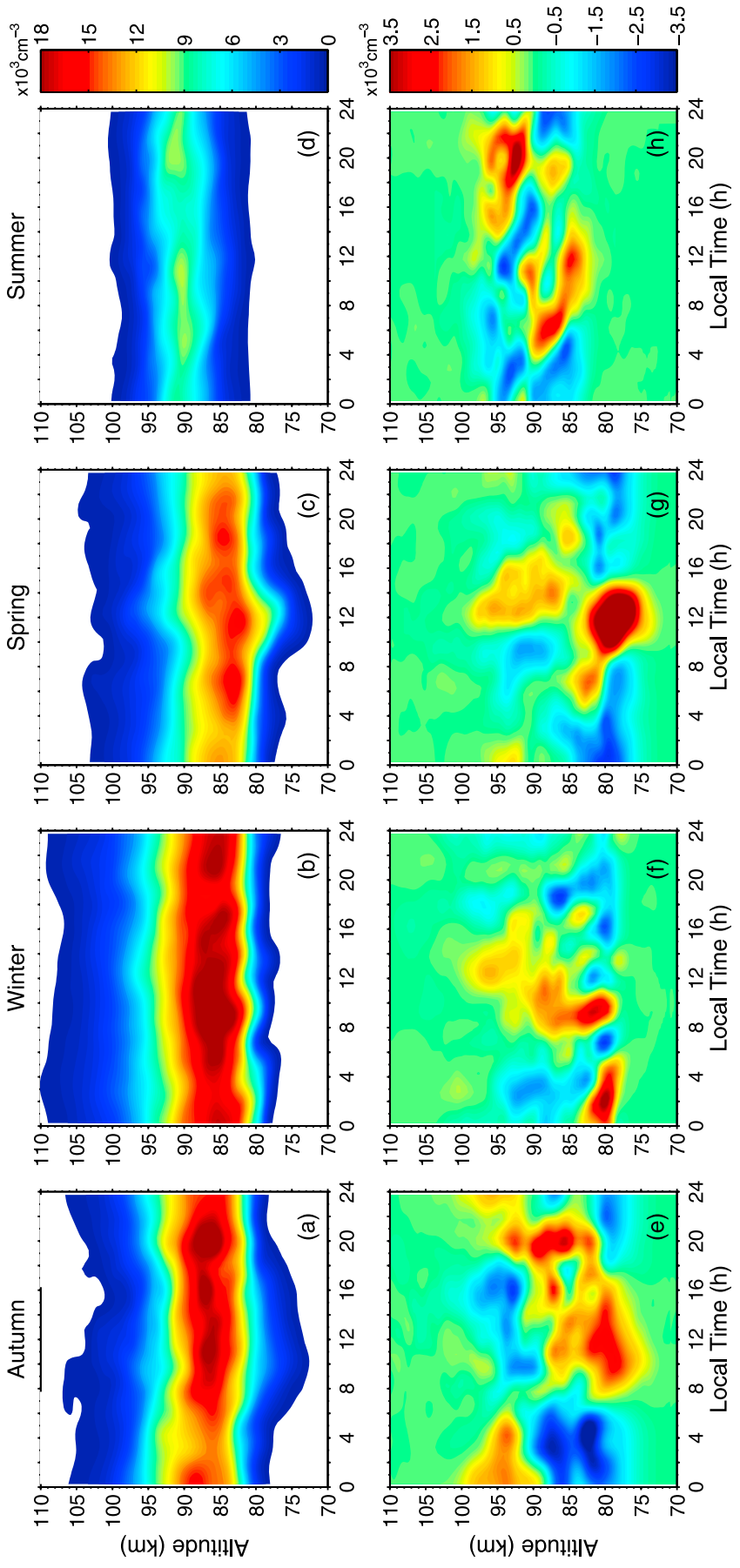
Autumn
Winter
Spring
Summer
(a)
(b)
(c)
(d)
(e)
(f)
(g)
(h)
Altitude (km)
Local Time (h)
x10^3cm^-3
18
15
12
9
6
3
0
3.5
2.5
1.5
0.5
−0.5
−1.5
−2.5
−3.5

Figure 2

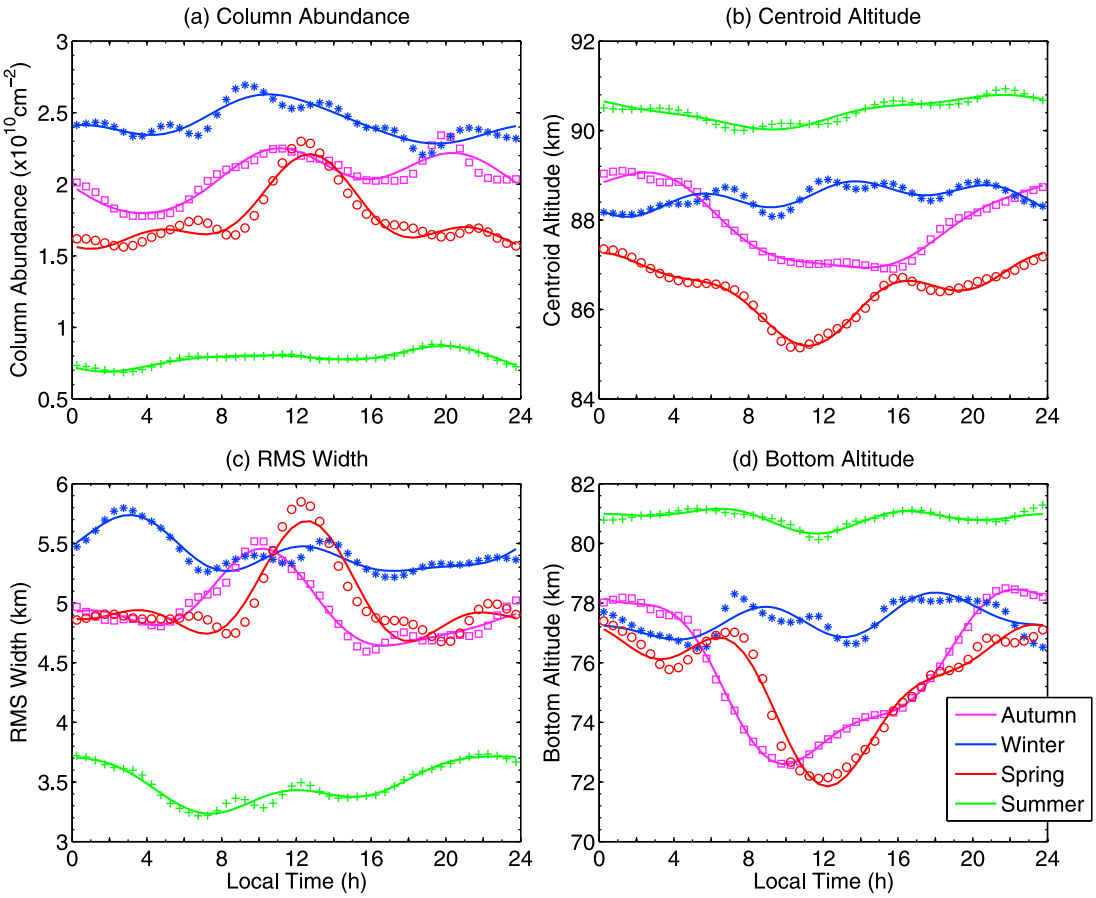

Figure 3. Diurnal variations of the Fe layer column abundance, centroid altitude, RMS width, and bottom altitude derived from the four seasonal composites (autumn: squares and pink curve; winter: stars and blue curve; spring: circles and red curve; summer: crosses and green curve). The solid curves are the harmonic fittings to the observational data points.

semidiurnal and terdiurnal oscillations. For the column abundance, the summer and winter seasons have comparable amplitudes of 24-h and 12-h oscillations, which are about 5% of the mean abundance of the corresponding seasons. The 24-h and 12-h oscillations in autumn are also comparable and about 7.3% of the mean abundance. The amplitude of 24-h oscillation in spring is ~13% of the mean abundance, double the amplitude of the 12-h oscillation. Springtime noon hours have higher column abundance and larger RMS width than those at night. The autumn column abundance and RMS width have weaker dependence on local time but in general larger noon values.

[15] Due to the largest difference of solar radiation between noon and midnight, the comparison of Fe profiles at these two local times can shed light on the roles of solar radiation in the diurnal variations. In Figure 4 we compare Fe density profiles at midnight and noon for the four seasons (i.e., 0 ± 0.5 LT and 12 ± 0.5 LT mean profiles). A distinct feature is the lower altitude and higher Fe density at the underside around noon than at midnight in autumn and spring. The altitude difference between the midnight and noon 300 cm^{-3} density contours is about 5 km in both seasons, while the difference at the 3000 cm^{-3} contour is 2.8 km in autumn and 3.8 km in spring. Such bottom growth leads to the scale height of Fe density below 80 km increasing from 0.5 to 1.5 km in the night to about 2–4 km at noon in autumn and spring. The midnight and noon profiles have much smaller differences on the bottomside in summer and are essentially identical in winter. On the layer topside, the noon upper boundary is lower than the midnight profile in autumn, but nearly identical to the midnight upper boundary in spring, summer and winter.

4. Solar Effects on the Fe Layer Bottomside

[16] The autumn and spring composite profiles clearly show diurnal variations of the Fe layer, and the daytime bottom extension appears to be correlated with solar illumination. Therefore, it is essential to investigate how the observed Fe diurnal variations are related to solar elevation

Figure 2. (a–d) Seasonal composite contours of Fe density versus local time and altitude, and (e–h) Fe density perturbations for autumn, winter, spring and summer seasons. Note that Fe densities below 300 cm^{-3} have been set to white in Figures 2a–2d. The density perturbations for summer in Figure 2h have been multiplied by a factor of 2 for better readability. The units for Fe densities and density perturbations are ×1000 cm^{-3}.

Table 3. Parameters of Harmonic Models for Diurnal Variations in Measured Fe Layer Column Abundances, Centroid Altitudes, RMS Widths and Bottom Altitudes at McMurdo, Antarctica Through Four Seasons[a]

	Autumn	Winter	Spring	Summer
	Column Abundance			
A_0	2.05 ± 0.02	2.43 ± 0.02	1.76 ± 0.02	0.78 ± 0.003
A_{24}	0.15 ± 0.02	0.12 ± 0.02	0.23 ± 0.02	0.043 ± 0.005
A_{12}	0.14 ± 0.02	0.08 ± 0.02	0.12 ± 0.02	0.050 ± 0.05
A_8	0.03 ± 0.02	0.02 ± 0.02	0.10 ± 0.02	0.016 ± 0.005
P_{24}	15.4 ± 0.5	10.2 ± 0.7	12.7 ± 0.4	16.0 ± 0.4
P_{12}	9.8 ± 0.3	11.4 ± 0.5	0.6 ± 0.4	8.1 ± 0.3
P_8	3.6 ± 0.9	0.8 ± 0.8	4.8 ± 0.3	4.5 ± 0.4
Correlation Coefficient	0.95	0.91	0.96	0.98
	Centroid Altitude			
A_0	87.9 ± 0.02	88.5 ± 0.05	86.4 ± 0.03	90.4 ± 0.02
A_{24}	1.07 ± 0.03	0.22 ± 0.05	0.75 ± 0.03	0.34 ± 0.03
A_{12}	0.09 ± 0.04	0.06 ± 0.05	0.27 ± 0.03	0.04 ± 0.03
A_8	0.12 ± 0.04	0.2 ± 0.05	0.23 ± 0.03	0.06 ± 0.03
P_{24}	1.2 ± 0.1	15.7 ± 0.9	23.6 ± 0.2	21.0 ± 0.4
P_{12}	2.8 ± 0.8	6.4 ± 1.6	4.0 ± 0.3	2.5 ± 1.9
P_8	3.9 ± 0.4	5.4 ± 0.3	7.5 ± 0.2	4.9 ± 0.8
Correlation Coefficient	0.99	0.89	0.99	0.95
	RMS Width			
A_0	4.94 ± 0.01	5.42 ± 0.02	5.0 ± 0.03	3.49 ± 0.01
A_{24}	0.25 ± 0.02	0.13 ± 0.02	0.26 ± 0.04	0.20 ± 0.02
A_{12}	0.21 ± 0.02	0.13 ± 0.02	0.27 ± 0.04	0.08 ± 0.02
A_8	0.07 ± 0.02	0.08 ± 0.02	0.16 ± 0.04	0.04 ± 0.01
P_{24}	8.8 ± 0.3	3.6 ± 0.2	12.2 ± 0.6	22.2 ± 0.3
P_{12}	10.6 ± 0.3	14.2 ± 0.3	12.6 ± 0.2	11.8 ± 0.3
P_8	2.1 ± 0.3	3.7 ± 0.3	4.6 ± 0.3	3.3 ± 0.5
Correlation Coefficient	0.98	0.94	0.95	0.98
	Bottom Altitude			
A_0	75.8 ± 0.03	77.4 ± 0.1	75.4 ± 0.1	80.9 ± 0.03
A_{24}	2.83 ± 0.05	0.36 ± 0.14	2.1 ± 0.1	0.17 ± 0.05
A_{12}	0.28 ± 0.05	0.43 ± 0.14	0.9 ± 0.1	0.21 ± 0.05
A_8	0.52 ± 0.05	0.33 ± 0.14	0.7 ± 0.1	0.17 ± 0.05
P_{24}	23.7 ± 0.1	17.2 ± 1.5	0.8 ± 0.2	0.9 ± 1.0
P_{12}	3.2 ± 0.3	7.6 ± 0.7	6.8 ± 0.3	5.4 ± 0.4
P_8	5.0 ± 0.2	1.2 ± 0.6	7.6 ± 0.2	7.6 ± 0.3
Correlation Coefficient	0.99	0.82	0.98	0.91

[a] A_0 is the diurnal mean, A_{24}, A_{12}, and A_8 are the amplitudes and P_{24}, P_{12}, and P_8 are the phases of the diurnal, semidiurnal and terdiurnal oscillations, respectively. Means and amplitudes for column abundance, centroid altitude, RMS width and bottom altitude are given in the units of $\times 10^{10}$ cm^{-2}, km, km and km, respectively; phases are in hours.

angles. This is done most effectively by analyzing individual days of observations to avoid artifacts caused by seasonal changes of solar elevation angle with local time. Here we present three case studies with continuous lidar observations spanning ~24 h at McMurdo. They represent three different solar illumination and MLT conditions. The solar elevation is defined as the angle from the horizon at sea level up to the geometric center of the Sun's apparent disk.

[17] Figure 5 shows contour plots of the Fe layer on 20–21 March 2012, 7–8 April 2011, and 11–12 August 2011. These three cases are 1, 17, and 40 days away from the autumn equinox (21 March) or spring equinox (21 September), respectively, so they represent quite different solar illuminations. The day and night switch in the MLT is clearly shown in all three cases, with the nighttime bottom around or slightly below 80 km and the daytime bottom extended to 70–73 km. The observations on 20–21 March 2012 start in the daytime under quite strong solar radiation. By ~19 LT the relatively wide Fe layer begins to "shrink" as the layer bottom starts to contract and reaches its nighttime high around 21 LT. After going through a relatively short night, the layer bottom begins to extend downward around 4 LT, and finishes the descent by 5 LT. Afterward, the layer bottom resides stably around 72–73 km throughout the remainder of the observations. The ascending rate at sunset appears to be slower than the descending rate at sunrise. For the 7–8 April 2011 case, growth is observed at the layer bottom during the morning hours around 6 LT when sunlight hits the MLT. The bottom altitude quickly descends to 72–73 km within an hour and then stays at this low altitude for ~10 h before ascending back to the night altitude around 17 LT. The ascending rate at dusk appears to be slower than the descending rate at dawn. The case on 11–12 August 2011 (Figure 5c) experiences the Sun below the horizon at sea level through the entire 25 h of observations, but sunlight reaches the MLT region for several hours around noontime. This situation is reflected in Figure 5c, where the bottom extension is very obvious around noon hours. This August case indicates that after long dark nighttime, the return of sunlight to the MLT region, even for only a few hours, can cause significant enhancement of Fe densities at the underside of the Fe layers. Interestingly, in this August case, the Fe layer bottom extends to nearly 70 km at noon, to our knowledge the lowest ever reported in the literature. The above three representative cases clearly show that the bottom growth/contraction of the Fe layer is a solar effect and not tidal in nature.

[18] To quantify the solar effects on the Fe layer bottomside, the bottom altitudes are plotted versus local time in Figures 6a–6c for the three cases. Here the bottomside of the Fe layer is defined as the altitude of the 300 cm^{-3} density contour. The minimum sunlit altitude and the solar elevation angle are plotted versus local time, respectively, as black and red curves in Figures 6d–6f. Here the minimum sunlit altitude refers to the lowest altitude that sunlight can reach for a given solar elevation, which is computed using a simple geometry model wherein sunlight is treated as parallel light and the Earth is treated as an ideal sphere. Note that the scales for solar elevations on the right side have different ranges for the 3 days. The bottom altitudes are also plotted versus their corresponding solar elevations in Figures 6g–6i.

[19] A striking feature is the nearly constant bottom altitudes during the day and during the night (excluding the transition periods from night to day or from day to night) revealed in the March and April cases (Figures 6a and 6b). The Fe layer bottom stays near 80 km in the night and around 72–73 km during the day quite stably, although the bottom altitude can still be perturbed by waves during the day and night as shown in Figures 6a–6c. The duration of the daytime flat bottom is closely correlated with the period of solar elevation above the horizon at sea level. The flat bottom around 72–73 km on 20–21 March 2012 lasts ~14 h from 5 to 19 LT, while it is ~10 h from 7 to 17 LT in the case of 7–8 April 2011. The period for solar elevation above the horizon is ~13 h from 5.5 to 18.5 LT for the March case and ~9 h from 7.5 to 16.5 LT for the April case. In both cases, the daytime flat bottom duration is about 1 h longer than the sunlit period above the horizon. This is illustrated by the bottom altitude

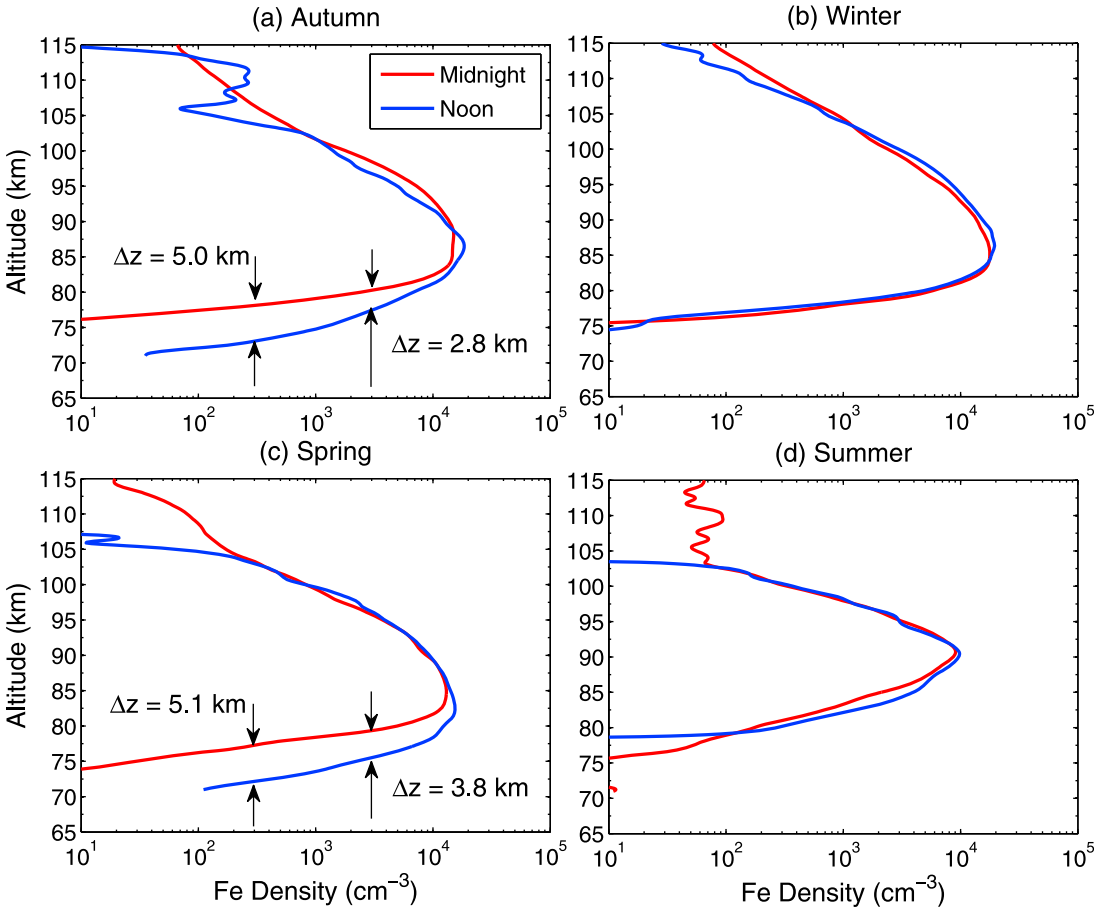

Figure 4. Comparison of Fe density profiles between noon and midnight through four seasons: (a) autumn, (b) winter, (c) spring, and (d) summer.

completing its descent about a half hour before sunrise and beginning its ascent about a half hour after sunset at sea level. These transition times correspond to solar elevations of around −1° to −2° according to Figures 6a, 6b, 6d, and 6e. In the August case, because the sun is never above the horizon on 11–12 August 2011 but below −2° through the entire observations (Figure 6f), the daytime is short at the MLT, leading to the continuously varying bottomside altitude around the noon hour in Figure 6c. It is also apparent in Figure 6 that the solar elevation angle at which the bottom altitude begins its descent from the nighttime high during sunrise, as well as completing its ascent to the nighttime high during sunset, is around −8°.

[20] The transition of bottom altitude occurs during dawn and dusk periods in a nearly linear fashion with local time in Figures 6a and 6b. Even for the August case in Figure 6c, the transitions can be simplified to linear variations in the first-order approximation. Linear fits to the transition periods provide the change rates of bottom altitude Z_B with time, dZ_B/dt, which are given in Table 4. The descent during sunrise is much faster than the ascent during sunset, confirming the asymmetry findings from Figure 5. For example, in the case of 20–21 March 2011, the sunrise descending rate dZ_B/dt is -5.0 ± 0.5 km/h, compared to the sunset ascending rate of 3.6 ± 0.2 km/h. Such asymmetry exists in all three cases. Comparing among these three cases, the ascending rate in the sunset exhibits a trend that the bottom transition takes the minimum time at the March equinox but becomes slower when the day of year moves away from the equinox. The descending rate of the April case is comparable or slightly faster than the March equinox case, while both are much faster than the descending rate on 11–12 August 2011.

[21] The bottom transition corresponds to solar elevation angles between −1° to −2° and −7° to −9° as shown in Figures 6g–6i, when sunlight intersects with the lower atmosphere before reaching the MLT. Here the lower atmosphere refers to the atmosphere below the MLT region, say below 70 km or lower. The absorption and scattering of sunlight by the lower atmosphere apparently influences the solar flux and spectrum that reach the MLT region, producing pronounced effects on the bottom growth/contraction. This transition shape is consistent in all three cases. It appears that the transition corresponds to certain solar elevations rather than fixed local time. This explains the near 'V' shape of the bottom altitudes derived from the autumn and spring composites (Figure 3d). Because the bottom transition is 'locked' to the solar elevation angle and the corresponding local time changes through the season, averaging the data in the same local time but with different solar elevations smears out the flat bottom feature on individual days, resulting in the 'V' shape. The bottom altitudes are plotted versus solar elevations in different colors in Figures 6g–6i for sunrise (0–12 LT) and sunset (12–24 LT).

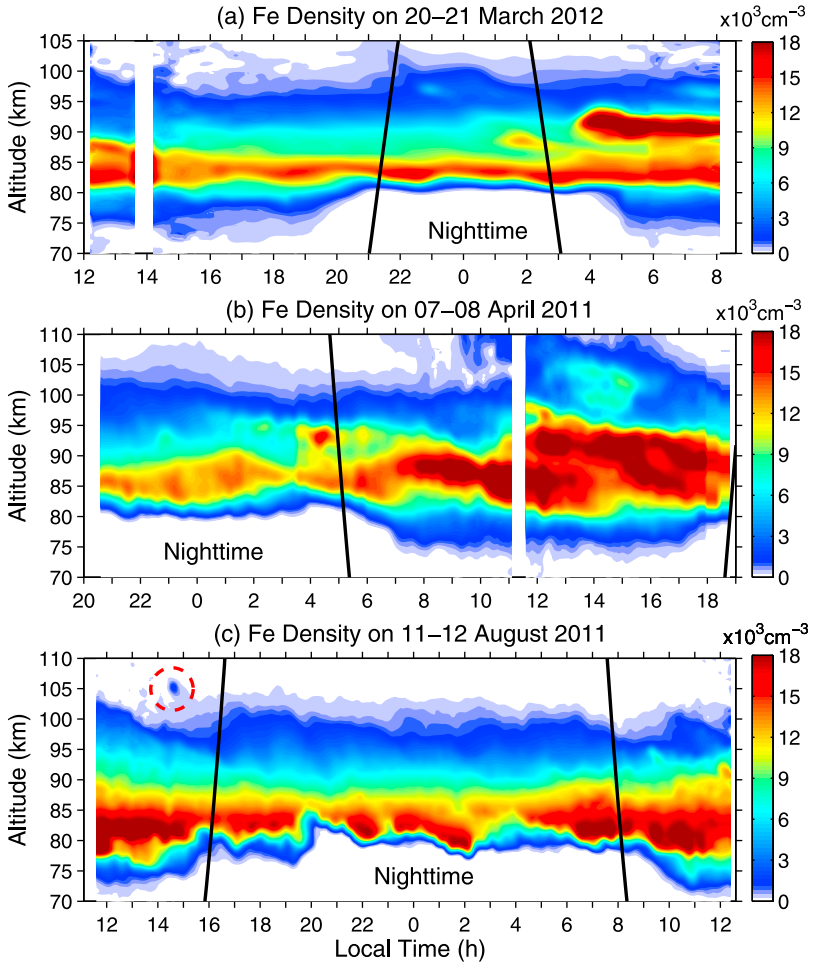

Figure 5. Contours of Fe density versus local time and altitude observed on (a) 20–21 March 2012, (b) 7–8 April 2011, and (c) 11–12 August 2011 at McMurdo, Antarctica. Black lines denote the minimum sunlit altitudes in the MLT region and the corresponding local time.

It is apparent that the bottom altitude change rate with solar elevation angle ($dZ_B/d\theta_E$) during sunrise is steeper than during sunset in all three cases. Although the August case exhibits an altitude shift downward as compared to the March and April cases, these three cases give similar sunrise rates or sunset rates, indicating that the rate with solar elevation does not change with season. To quantify the rates, linear fits are applied to the transition periods. Because the April case experienced large wave perturbations, the fit is limited to a smaller range than the other two cases in order to minimize the wave influences. The results of $dZ_B/d\theta_E$ are listed in Table 4. On average the rate during sunrise is about −1.6 km/deg, steeper than the average rate of about −1.0 km/deg during sunset. The rate difference is consistent with the descent-ascent asymmetry observed above.

[22] To further study the bottom transition, we investigate how fast the Fe layers respond to sunrise and sunset at the MLT. The minimum sunlit altitudes plotted as black lines in Figures 5 and 6 denote the sunrise and sunset times for each altitude in the MLT. The refraction of sunlight by the Earth's atmosphere introduces time correction less than 10 min, and is thus negligible for the purpose of this study. When sunlight first reaches the Fe layer bottom at 78–80 km during sunrise, the corresponding solar elevation is about −9° in all three cases, regardless the day of year or latitude. However, the Fe layer bottom descent does not start until the solar elevation rises to about −8°. Therefore, there are considerable time delays between sunrise at the MLT and appreciable Fe density growth at the bottom. As shown in Figure 7, such time delays increase with decreasing altitude. Using the March equinox case as an example, the sunrise at 79 km is 2.83 LT in Figure 6d, but the bottom descent starts at 3.9 LT from this altitude (Figure 6a), giving a delay time of ∼1.07 h (Figure 7). The sunrisetime at 75 km is 2.93 LT, and the Fe density at 75 km increases to 300 cm^{-3} at 4.85 LT, giving the time delay of 1.92 h. Such delay time also varies with the season, e.g., the time delay at 75 km changes to 1.6 h on 7–8 April 2011 and 0.97 h on 11–12 August 2011. On the other hand, the bottom density starts to decrease a few hours before sunset at MLT altitudes. The sunset time difference also varies with season, being shortest in the August case and longest in the March case. For example, the Fe density starts to decrease about 1.7, 1.4, and 0.45 h before the sunset at 75 km in the March, April, and August cases, respectively. As with sunrise, the lower altitudes experience longer time differences at sunset in all three cases (Figure 7).

[23] The noon and midnight Fe density profiles are compared for the three case studies in Figure 8. The noon bottom

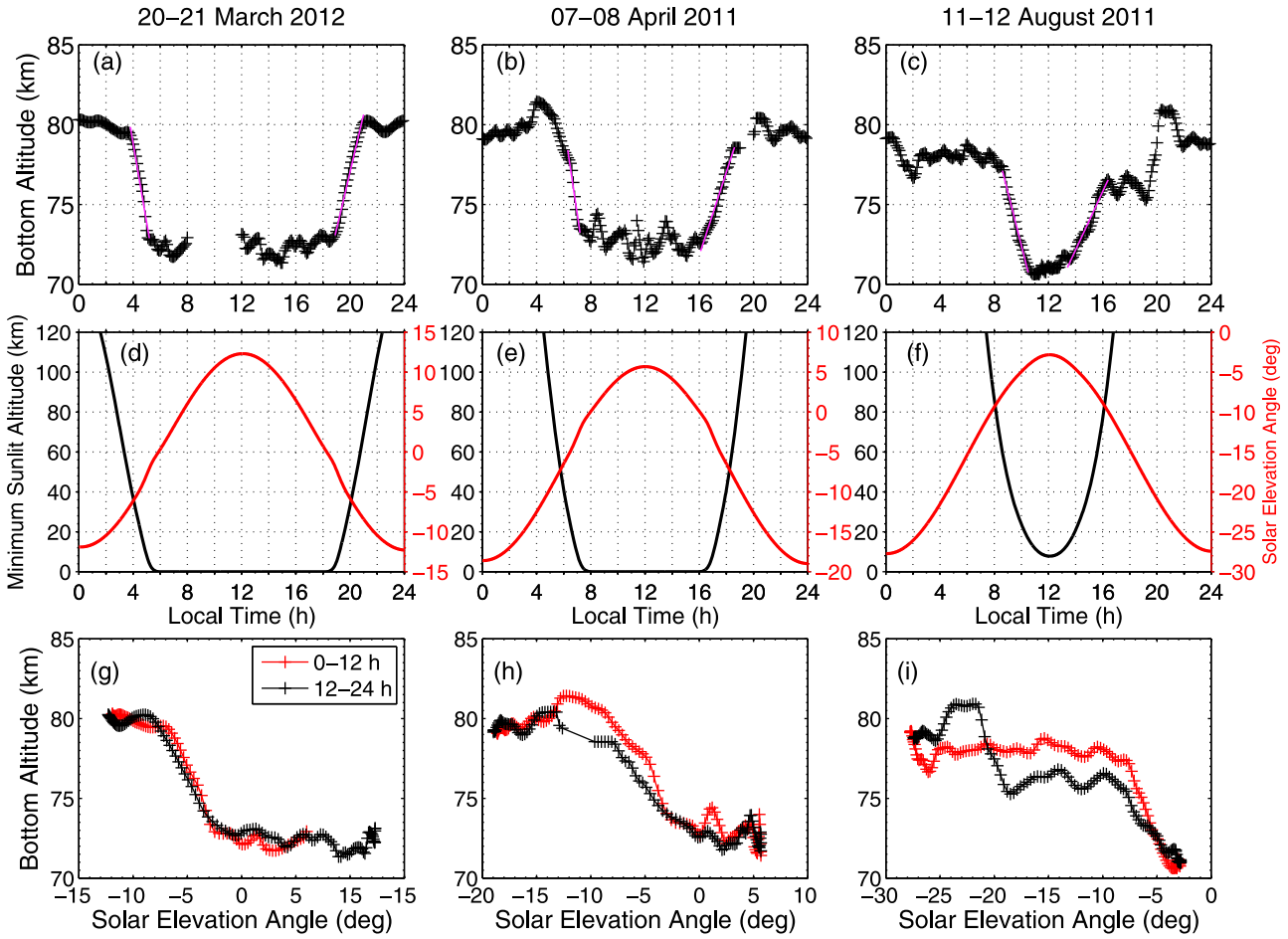

Figure 6. (top) Fe layer bottom altitudes versus local time, (middle) the corresponding minimum sunlit altitude and solar elevation angle, and (bottom) the bottom altitudes versus solar elevation angle for the lidar observations on (a, d, g) 20–21 March 2012, (b, e, h) 7–8 April 2011, and (c, f, i) 11–12 August 2011. The black and red lines in Figures 6d–6f represent the minimum sunlit altitude and solar elevation angle, respectively. The purple lines in Figures 6a–6c are linear fits to the transition periods at dawn and dusk. The red and black crosses in Figures 6g–6i are for sunrise (0–12 h) and sunset (12–24 h), respectively.

extensions are substantial in all cases, and they are very significant on 11–12 August 2011 when the altitude difference is as large as ~8 km for the density of 300 cm^{-3}. The noon profiles have consistently higher density and lower altitude at the layer peak than the midnight profiles. Both the April and August cases exhibit enhancement of the layer topside at noon as compared to midnight. Checking the topside altitude of the 300-cm^{-3} Fe density contour, all three cases show neither local time nor solar elevation dependence. The upward extension of the topside around noon on 7–8 April 2011 is likely caused by a high-altitude sporadic Fe layer event, whereas the August case lacks sporadic activity. We note that 11 August 2011 was close to the peak time of Perseids meteor shower, and in fact our lidar observed a meteor trail, shown as a dot around 14.5 LT and near 105 km in Figure 5c. Such a meteor shower may impact the layer topside through enhanced direct meteor deposition.

5. Conclusions and Discussion

5.1. Observational Conclusions

[24] The McMurdo Fe layer undergoes significant diurnal variations on the bottomside below 80 km in autumn and spring when this region experiences appreciable diurnal

Table 4. Transition Rates of Fe Layer Bottom Altitude With Local Time and Solar Elevation[a]

	dZ_B/dt (km/h)			$dZ_B/d\theta_E$ (km/deg)		
	20 Mar 2012	7 Apr 2011	7 Aug 2011	20 Mar 2012	7 Apr 2011	11 Aug 2011
Sunrise	−5.0 ± 0.5	−5.4 ± 1.0	−3.4 ± 0.2	−1.54 ± 0.14	−1.70 ± 0.30	−1.75 ± 0.08
Sunset	3.6 ± 0.2	2.6 ± 0.2	1.8 ± 0.1	−1.18 ± 0.04	−0.94 ± 0.10	−0.92 ± 0.06
Correlation[b]	0.99/0.99	0.98/0.99	0.99/0.98	0.99/0.99	0.97/0.99	0.99/0.99

[a]Notation: Z_B – bottom altitude, t – local time, and θ_E – solar elevation angle.
[b]The first and second numbers are the correlation coefficients for sunrise and sunset fittings, respectively.

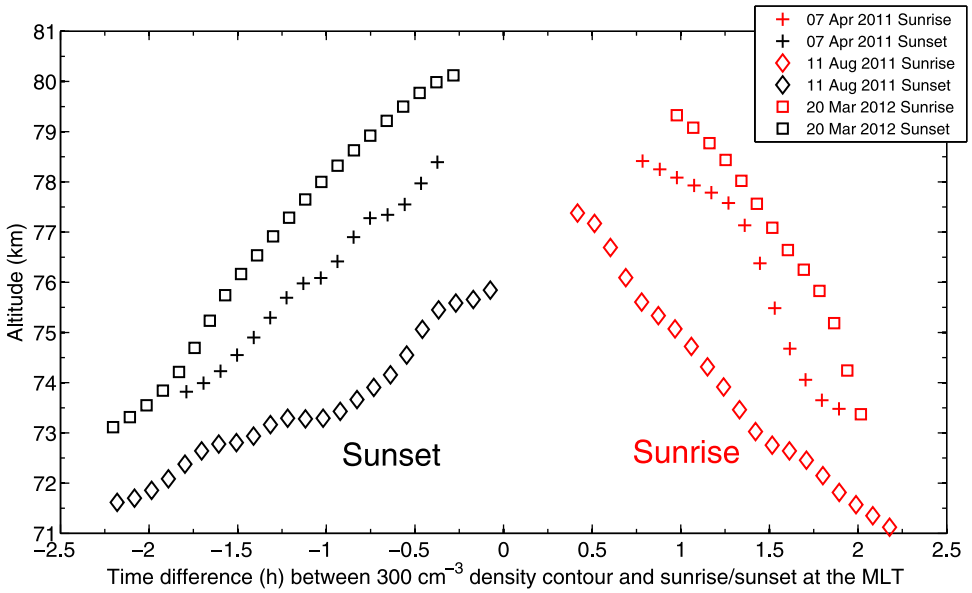

Figure 7. Time difference between the 300 cm^{-3} Fe density contour and sunrise/sunset at the corresponding MLT altitude for the three cases in March (squares), April (crosses), and August (diamonds). Positive time differences are for the bottom extension during the sunrise and negatives are for the bottom contraction during the sunset.

variations of solar illumination. The lidar observations show that the bottomside of the Fe layer extends downward by ~5 km or more during the day, and then contracts at night. In the polar winter with 24-h darkness, the Fe layer bottom altitudes are strongly perturbed by waves, but they are not tied to local time or solar elevation. The Fe density perturbations exhibit downward phase progression in the summer main layer (84–98 km) with a vertical phase speed of about −1.25 km/h. These are most likely due to diurnal and semidiurnal tidal perturbations. The other three seasons do not show clear tidal signatures in the main layers, and the density perturbations are dominated by residual gravity wave perturbations. Around the layer peak (~84–90 km), the Fe density undergoes substantial variations throughout the day in each season with a tendency to higher peak density around local noon and lower density near local midnight. Summer Fe layers show lower density, higher altitude, and narrower width than those of the other three seasons, principally because of heterogeneous removal of Fe atoms below 90 km by ice particles, low temperature, and upward advective transport in the polar summer MLT.

[25] The case studies with 24-h continuous lidar observations in March, April and August clearly demonstrate that the diurnal variations at the Fe layer bottomside are closely correlated with solar elevation angle. The bottomside growth/contraction of the Fe layer is not related to any obvious tidal or wave effect, whereas it is clearly revealed as a solar effect. The layer bottomside altitudes (i.e., constant

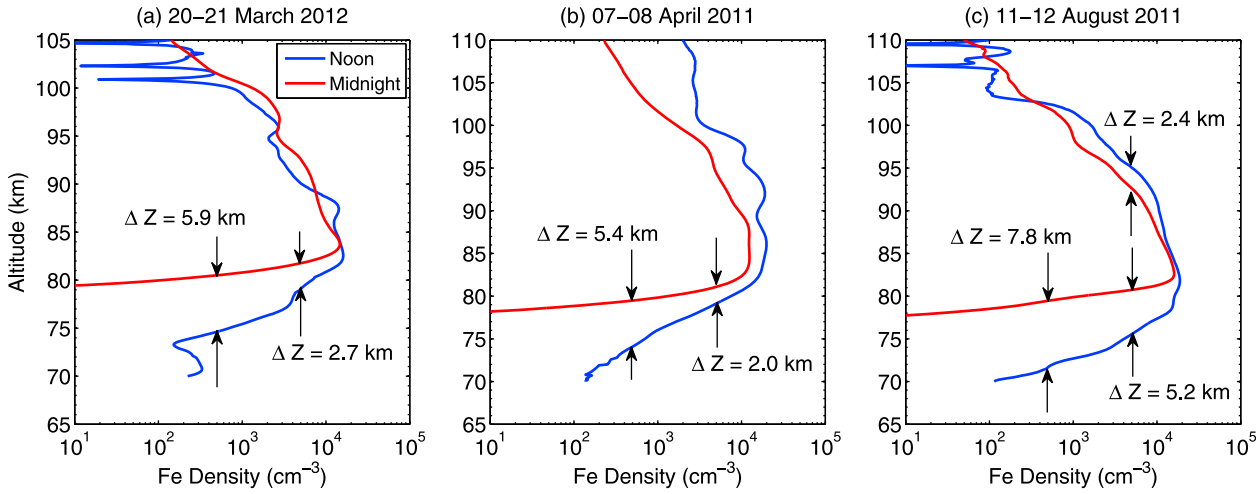

Figure 8. Comparison of Fe density profiles between noon and midnight on (a) 20–21 March 2012, (b) 7–8 April 2011, and (c) 11–12 August 2011.

density contours) are nearly flat during both day and night in the March and April cases. The duration of the daytime flat bottom is closely correlated with the period of solar elevation above the horizon. The bottom extension occurs even when the MLT is only sunlit for a few hours as in the August case, but is absent through the dark polar winter nights. The bottom transition occurs when the solar elevation angles are between -9° and -1° as measured from sea level. That is when sunlight illuminates the MLT region after first passing through the lower atmosphere. Once the solar elevation is above -1°, the layer bottomside is stable at its daytime altitude ($\sim$70–73 km) and density ($\sim$200–500 cm^{-3}). Similarly, once the solar elevation falls below -9°, the layer bottomside is stable at its nighttime altitude ($\sim$78–80 km).

[26] The transition of bottom altitude occurs during dawn and dusk in a nearly linear fashion with local time. Asymmetry exists between the bottom downward extension at dawn and the upward contraction at dusk. In general the descending (formation) rate is faster than the ascending (dissipation) rate. The bottom ascent during sunset takes the minimum time at the March equinox and becomes slower when moving away from the equinox. However, the descending rates during sunrise are comparable between the March and April cases, and both are much faster than the August case when the Sun stays below the horizon at sea level. The rate of change of the bottom altitude with solar elevation angle ($dZ_B/d\theta_E$) does not vary with season, and the average rate of about -1.6 km/deg during sunrise is steeper than the rate of -1.0 km/deg during sunset. There is a time delay between sunrise at the MLT and appreciable bottomside growth. Conversely, the contraction of the layer bottomside starts earlier than MLT sunset. Such time delays vary with altitude and season. For a given day, it takes a longer time to produce appreciable changes in Fe bottomside density at the lower altitudes than at higher altitudes. For a fixed altitude, the delay time is longest on 20–21 March, intermediate on 7–8 April and shortest on 11–12 August when the daily mean solar elevation varies from the highest to the lowest.

[27] Finally, the bottom enhancement during the day leads to the noon profile having higher peak and bottom densities, as well as lower peak and bottom altitudes, than the midnight profile. This is true for the autumn and spring composites as well as in three individual case studies. A direct consequence is that the noon profiles possess larger scale heights of Fe density on the underside than the midnight profiles in autumn and spring. The autumn composite profiles exhibit a small reduction in Fe density on the layer topside at noon, but such a reduction is not pronounced in the spring composite. Furthermore, the topside altitudes (constant density contours) show neither local time nor solar elevation dependence in the three individual cases.

[28] In summary, significant solar effects in diurnal variations of the Fe layer are observed at McMurdo, and the daytime bottomside extension is clearly correlated with the solar elevation. The observed Fe diurnal variations are obviously much larger than the Na diurnal variations reported in the literature. These results provide direct evidence for the influence of solar UV radiation on the chemistry and composition of the mesopause region.

5.2. Implications for Fe Chemistry in the MLT

[29] Although this is the first formal report of significant diurnal variations of the Fe layer to appear in the scientific literature, we are aware that J. Höffner has observed a similar daytime extension of the Fe layer bottomside at Andoya from 2008 to 2009 (J. Höffner, private communication, 2012). In addition, our group also observed this same feature at Boulder, Colorado in August and September 2010 when testing this lidar prior to its McMurdo deployment. Unfortunately, existing modeling work has not addressed the potential impact of varying solar illumination on Fe layer densities. Nevertheless, *Plane* [2004] presented a comprehensive modeling of Na diurnal variations, which serves as a guideline in the discussion.

[30] At the underside of the Fe layer, FeOH is believed to be the major reservoir species. Partitioning among Fe, FeOH and other Fe-containing species is largely determined by the ratio of [O], [H] and [O_3]. Fe is converted to the relatively stable reservoir FeOH through a series of reactions beginning with oxidation of Fe by O_3. FeO and FeO_2 produced by this oxidation are short-lived according to *Self and Plane* [2003]. They can be recycled back to Fe by atomic O or further converted to reservoir species via reactions with H_2O, CO_2 and O_2. FeOH is recycled back to Fe by reaction with H. Therefore, the Fe layer density and shape on the bottomside are strongly dependent on the concentration profiles of [H], [O] and [O_3]. Atomic O and H are produced during the day by photolysis of O_2 and H_2O, respectively. Above 82 km there is little diurnal variation in these species, but below 80 km the atomic O and H concentrations increase by about 4–5 orders of magnitude from night to day [*Rodrigo et al.*, 1991; *Plane*, 2003]. The sharp transition between 75 and 85 km at night corresponds to the well-known atomic oxygen shelf. As a consequence, FeOH is converted back to Fe much faster during the day while the loss of Fe via reaction with O_3 is slower during the day than at night. Therefore, we believe the observed bottomside extension during the day is a direct consequence of Fe being produced from FeOH, because of the much higher O and H concentrations. Furthermore, by analogy with Na diurnal variations, photolysis of Fe-containing molecules (e.g., FeOH) under sunlight, if any, can help enhance the daytime growth and extension on the layer bottomside.

[31] However, the situation is not as simple as described above, which assumes a large supply of FeOH near the layer bottomside. The potential removal of FeOH and other Fe species must also be considered here. In principle, Na species have similar partitioning among Na, $NaHCO_3$ and other Na-containing molecules. If the cycling between Na and Na-containing molecules is a closed system, a large diurnal variation of Na should also be observed [see *Plane*, 2004, Figure 4a]. That is, the noon Na profile should be lower in height and much larger in density than the midnight profile. Because earlier Na observations did not show such large diurnal variations [*Clemesha et al.*, 1982; *States and Gardner*, 1999], *Plane* [2004] suggests that the reservoir species $NaHCO_3$ is removed via dimerization of $NaHCO_3$ and permanent attachment of the Na species on meteoric smoke particles. Such removal diminishes the concentration of $NaHCO_3$ that accumulate during the night. Therefore,

when sunlight returns to the MLT, the release of Na from $NaHCO_3$ is significantly reduced in comparison to the situation when no removal mechanisms are implemented. Because Fe diurnal variations are significant in the McMurdo observations, there must be appreciable FeOH concentrations at the underside of the Fe layer when sunlight returns. One implication is that the removal of FeOH and other reservoir species may not be as extensive as the removal of $NaHCO_3$. Nevertheless, the permanent removal of Fe or Na species by meteor smoke particles is unavoidable in order to balance out the meteoric input. The permanent removal rate of Na species is unlikely much higher than that of Fe species considering the ratio of Na/Fe in the MLT. It is possible that other removal mechanisms, e.g., via dimerization, are significant in removing $NaHCO_3$ but not so for the Fe species.

[32] The photolysis of O_2 and H_2O to produce O and H requires UV solar radiation, viz, the Lyman-α at 121.6 nm for breaking H_2O and the Schumann bands for breaking O_2. It is likely that the photolysis of FeOH and other Fe species also requires UV sunlight. It is well known that water vapor and ozone in the lower atmosphere efficiently absorb the UV sunlight over a large spectral range. For the period when solar elevation lies between $-1°$ and $-9°$, sunlight passes through the lower atmosphere before reaching the MLT. Therefore, the solar flux in the UV spectrum received at the MLT is attenuated. Within this elevation range, for the transition from night to day, the higher solar elevation leads to a shorter path through the lower atmosphere and thus, larger UV solar flux $\Phi(\lambda)$ reaching the layer bottomside below 80 km. Consequently, the photolysis rate of FeOH increases with time, which is given by $R_{photolysis} = \int\sigma(\lambda)\Phi(\lambda)d\lambda$ (in the unit of s^{-1}), where $\sigma(\lambda)$ is the photolysis cross section at wavelength λ [*Self and Plane*, 2002]. The increased photolysis of H_2O results in higher [H] thus higher release rate of Fe from FeOH, which is given by $R_H = k[H]$ (in the unit of s^{-1}), where k is the rate coefficient for the reaction of $FeOH + H \rightarrow Fe + H_2O$. Overall the production rate of Fe—given by $(R_{photolysis} + R_H)[FeOH]$ in the unit of $cm^{-3}\ s^{-1}$—increases as the Sun rises from solar elevation of $-9°$. On the other hand, the loss rate of Fe via reaction with O_3 is given by $k[O_3]$ in the unit of s^{-1}, but it is competed by the reaction of $FeO + O \rightarrow Fe + O_2$. As there is no appreciable [Fe] on the bottomside at night, the total loss rate of $k[O_3][Fe]$ (in the unit of $cm^{-3}\ s^{-1}$) at the beginning of the transition is close to zero. Once the [Fe] starts to build up, the total loss rate will increase with time during the transition, eventually matching the simultaneously increasing production rate of Fe. Fe density will continue increasing until the production rate and the loss rate reach a balance, after which the Fe density will remain at the daytime steady state. As long as sunlight propagates above the lower atmosphere before reaching the MLT, it is not strongly absorbed by water vapor or ozone. Therefore, the UV solar flux reaching the MLT remains nearly constant (to first order) once above $-1°$ at dawn until the sun sets below $-1°$ at dusk. Constant UV solar flux leads to the constant concentration of O, H, and O_3 and constant photolysis of FeOH or other Fe-containing species. As a consequence, the production and loss of Fe reach a balance at the underside, leading to the nearly constant bottom altitude during the daytime period of the solar elevation above $-1°$. Once the Sun sets below $-9°$, sunlight is totally blocked by the Earth from reaching the MLT. The concentrations of O and H dramatically decrease in the absence of UV light and the photolysis of Fe species stops. Thus, the production of Fe on the underside is significantly reduced and the density reaches a new balance with the loss of Fe at higher altitude ($\sim$80 km) in the night. Consequently, the nighttime bottomside resides at the higher altitude around 80 km and the daytime bottomside resides at lower altitude around 72 km. Furthermore, the bottomside altitudes are quite stable during both day and night, although they are still susceptible to wave and tidal perturbations. In the above picture, factors like meteor ablation, transport and permanent removal by smoke particles are neglected in the transition time scale of 1–3 h. However, these factors are important in determining the steady state Fe densities among different seasons.

[33] For any given altitude at the bottomside during the transition period, appreciable Fe density increase will not be observed until after sufficient integration time to build up Fe density to detectable levels (e.g., 100–300 cm^{-3}). Therefore, there is a time delay between sunrise and the 300 cm^{-3} Fe density contour. For the same day but at different altitudes, Fe loss via oxidation with O_3 increases substantially with decreasing altitude because the concentration of O_3 increases with decreasing altitude [*Rodrigo et al.*, 1991]. A consequence is that longer build-up time is required to produce detectable Fe density at lower altitude. According to *Helmer et al.* [1998], the [FeOH] concentration increases with decreasing altitude, while the photolysis rate is quite constant through the MLT altitudes according to *Self and Plane* [2002]. As a result, the Fe production by photolysis of FeOH increases with decreasing altitude at the underside. The Fe production via FeOH being recycled back by H and O can have either increasing or decreasing altitude dependence depending on the actual H, O and FeOH concentration profiles [*Rodrigo et al.*, 1991; *Plane*, 2003]. To first order, the production rate of Fe may be comparable in the altitude range of 70–80 km. The increasing loss is therefore likely the major factor determining the increasing time delay at lower altitude.

[34] The transition rate from higher to lower altitudes at the bottomside is affected by $d\theta_E/dt$, the rate of change of solar elevation with local time. Since the UV solar flux at the same solar elevation but on different days of year should be the same on the first order of approximation, smaller $d\theta_E/dt$ slows down the increase of UV solar flux thus the Fe production rate at the layer bottomside. This leads to longer transition time and lower transition rate dZ_B/dt. The variation of $d\theta_E/dt$ with season may explain the different transition rates in Table 4. In all three cases the transition time ($\sim$1.3 h) for solar elevation to rise from $-9°$ to $-6°$ is similar according to Figure 6d–6f; however, from $-6°$ to $-3°$, it takes $\sim$2 h on 11–12 August but only $\sim$0.9 h on 20–21 March. The $d\theta_E/dt$ slows down significantly during the later half of the sunrise transition in the August case, which is consistent with the August transition rate being the slowest.

[35] Besides $d\theta_E/dt$ affecting the increasing rate of Fe production rate, several other factors can also influence the seasonal change of the transition rate and time delay: the

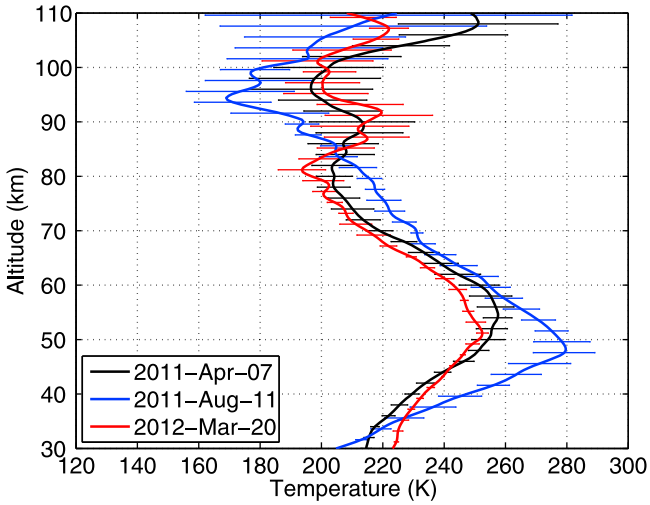

Figure 9. Comparison of SABER temperatures among 20–21 March 2012, 7–8 April 2011, and 11–12 August 2012. SABER version 1.07 data are used in this comparison. The horizontal bars on each curve represent the geophysical variability on the observational day.

history of FeOH, the temperature in the MLT, and the concentration of H_2O and O_3. The accumulation of FeOH over long dark polar nights coupled with downward transport results in higher FeOH concentration in August than in March or April, so more Fe atoms can be released even when sunlight only returns for several hours. At the same time, the rate coefficients of the reaction of FeOH with H are higher at higher temperatures, and the photolysis cross sections are most likely larger at warmer temperature based on the study of photolysis of Na species [*Self and Plane*, 2002]. Due to the insufficient signal-to-noise ratio, the Fe Boltzmann lidar cannot provide reliable temperatures between 70 and 80 km that are relevant to the current discussion. We can, however, use temperature profiles from the TIMED-SABER instrument, taking the mean of McMurdo overpasses within a range of $\pm5^\circ$ in latitude and $\pm10^\circ$ in longitude during the same period of lidar observations. Using the results of SABER v1.07 data in Figure 9, we find that the temperatures of 11–12 August 2011 are on average 10–20 K warmer than those of 7–8 April 2011 while the temperatures on 20–21 March 2012 are ~5 K colder than those of the April case in the altitude range of 70–80 km. Thus, the release of Fe from FeOH or other Fe-containing species is expected to be fastest on 11–12 August 2011 and slowest on 20–21 March 2012. Therefore, the 11 August case is expected to have a much shorter time delay, just as observed. Furthermore, the seasonal change of H_2O concentration below 80 km can affect the increased production of [H] via photolysis, and thus an increase of Fe production rate. If the concentration of O_3 varies with season, e.g., if $[O_3]$ in August is lower than in March or April, the Fe loss can be much smaller in August, helping the August case to build up appreciable Fe density faster as compared to March and April. Overall it is the magnitude of the net production rate of Fe (the difference between the Fe production and loss rates) and its variation during the transition period (solar elevation of -9° to -1°) that determine how fast the bottomside Fe density increases to a detectable level, thereby determining the transition time and build-up time observed. Although the photolysis rates of FeOH, O_2, and H_2O are symmetric with respect to solar elevations, the loss rates of H, O, and Fe at dawn and dusk are not symmetric. Neither are the variations of O_3 concentration. Therefore, it is not surprising to observe the asymmetry between the bottomside descent and ascent.

[36] Constituent vertical transport can have profound influences on the Fe layers and its diurnal variations [*Gardner and Liu*, 2010]. Advective transport certainly contributes to the stark contrast between the summer and winter layers, as the upwelling advection in summer helps lift the layer upward while the downwelling advection in winter pushes the layer downward [*Gardner et al.*, 2005]. The MLT above McMurdo experiences strong gravity wave activity throughout the year. Whether these waves introduce large dynamical, chemical and eddy transports and how they influence the Fe layers and their diurnal variations are largely unknown. Furthermore, none of the photochemical reaction rates of Fe-containing species have been reported in the literature except the photoionization rate of Fe [*Brown*, 1973; *Nahar et al.*, 1997]. The FeOH, O, H, and O_3 concentration profiles are also important to the quantitative modeling of the Fe diurnal variations, along with the rate coefficients of many neutral and ion chemical reactions associated with Fe. Many unknowns exist as roadblocks to the comprehensive understanding of the Fe diurnal variations and Fe chemistry in the MLT. Future lidar observations, laboratory measurements, and detailed modeling work are required to resolve these uncertain terms and to explain the observed Fe diurnal variations quantitatively and unequivocally.

[37] **Acknowledgments.** We sincerely acknowledge Zhangjun Wang, John A. Smith, and Cao Chen for their contributions to the McMurdo lidar campaign. We are very grateful to Chester S. Gardner for his valuable comments and suggestions, to John M. C. Plane for the valuable discussions on Fe chemistry, and to Jonathan S. Friedman for his valuable comments and English editing. We appreciate Allen Jordan and Barbara Emery for their assistance in the solar elevation calculation. Solar elevation angle was calculated using "sun_position.m" MatLab code developed by National Renewable Energy Laboratory. We sincerely acknowledge James Russell III and SABER team for providing the SABER temperature data. We thank the staff of United States Antarctic Program, McMurdo Station, Antarctica New Zealand and Scott Base for their support. This project was supported by the National Science Foundation (NSF) grant ANT-0839091.

References

Alpers, M., J. Höffner, and U. von Zahn (1990), Iron atom densities in the polar mesosphere from lidar observations, *Geophys. Res. Lett.*, *17*, 2345–2348, doi:10.1029/GL017i013p02345.

Alpers, M., J. Höffner, and U. von Zahn (1994), Sporadic Fe and E Layers at Polar, middle, and low latitudes, *J. Geophys. Res.*, *99*(A8), 14,971–14,985, doi:10.1029/94JA00589.

Baggaley, W. J. (2002), Radar observations, in *Meteors in the Earth's Atmosphere*, edited by E. Murad and I. P. Williams, pp. 123–148, Cambridge Univ., Cambridge, U. K.

Bowman, M. R., A. J. Gibson, and M. C. W. Sandford (1969), Atmospheric sodium measured by a tuned laser radar, *Nature*, *221*, 456–457, doi:10.1038/221456a0.

Broadfoot, A. L., and A. E. Johanson (1976), Fe (3860 Å) Emission in the Twilight, *J. Geophys. Res.*, *81*(7), 1331–1334, doi:10.1029/JA081i007p01331.

Brown, T. L. (1973), The chemistry of metallic elements in the ionosphere and mesosphere, *Chem. Rev.*, *73*, 645–667, doi:10.1021/cr60286a003.

Ceplecha, Z., J. Borovicka, W. G. Elford, D. O. Revelle, R. L. Hawkes, V. Porubcan, and M. Simek (1998), Meteor phenomena and bodies, *Space Sci. Rev.*, *84*, 327–471, doi:10.1023/A:1005069928850.

Chen, C., X. Chu, Z. Yu, W. Fong, A. McDonald, X. Lu, and W. Huang (2012), Lidar and radar investigation of gravity wave intrinsic properties

at McMurdo, Antarctica, paper presented at the 26th International Laser Radar Conference, ESA, Porto Heli, Greece, 25–29 June.

Chu, X., and G. Papen (2005), Resonance fluorescence lidar for measurements of the middle and upper atmosphere, in *Laser Remote Sensing*, edited by T. Fujii and T. Fukuchi, pp. 179–432, CRC, Boca Raton, Fla., doi:10.1201/9781420030754.ch5.

Chu, X., G. Papen, W. Pan, C. S. Gardner, and J. Gelbwachs (2002), Fe Boltzmann temperature lidar: Design, error analysis, and first results from the North and South poles, *Appl. Opt.*, *41*, 4400–4410, doi:10.1364/AO.41.004400.

Chu, X., W. Huang, W. Fong, Z. Yu, Z. Wang, J. A. Smith, and C. S. Gardner (2011a), First lidar observations of polar mesospheric clouds and Fe temperatures at McMurdo (77.8°S, 166.7°E), Antarctica, *Geophys. Res. Lett.*, *38*, L16810, doi:10.1029/2011GL048373.

Chu, X., Z. Yu, C. S. Gardner, C. Chen, and W. Fong (2011b), Lidar observations of neutral Fe layers and fast gravity waves in the thermosphere (110–155 km) at McMurdo (77.8°S, 166.7°E), Antarctica, *Geophys. Res. Lett.*, *38*, L23807, doi:10.1029/2011GL050016.

Chu, X., Z. Yu, C. Chen, W. Fong, W. Huang, C. S. Gardner, Z. Wang, B. Roberts, and J. A. Smith (2012), McMurdo lidar campaign: A new look into polar upper atmosphere, paper presented at the 26th International Laser Radar Conference, ESA, Porto Heli, Greece, 25–29 June.

Clemesha, B. R., D. M. Simonich, P. P. Batista, and V. W. J. H. Kirchhoff (1982), The diurnal variation of atmospheric sodium, *J. Geophys. Res.*, *87*(A1), 181–186, doi:10.1029/JA087iA01p00181.

Gardner, C. S., and A. Z. Liu (2010), Wave-induced transport of atmospheric constituents and its effect on the mesospheric Na layer, *J. Geophys. Res.*, *115*, D20302, doi:10.1029/2010JD014140.

Gardner, C. S., G. C. Papen, X. Chu, and W. Pan (2001), First lidar observations of middle atmosphere temperatures, Fe densities, and polar mesospheric clouds over the north and south poles, *Geophys. Res. Lett.*, *28*, 1199–1202, doi:10.1029/2000GL012622.

Gardner, C. S., J. M. C. Plane, W. Pan, T. Vondrak, B. J. Murray, and X. Chu (2005), Seasonal variations of the Na and Fe layers at the South Pole and their implications for the chemistry and general circulation of the polar mesosphere, *J. Geophys. Res.*, *110*, D10302, doi:10.1029/2004JD005670.

Gardner, C. S., X. Chu, P. J. Espy, J. M. C. Plane, D. R. Marsh, and D. Janches (2011), Seasonal variations of the mesospheric Fe layer at Rothera, Antarctica (67.5°S, 68.0°W), *J. Geophys. Res.*, *116*, D02304, doi:10.1029/2010JD014655.

Gelbwachs, J. A. (1994), Iron Boltzmann factor lidar: Proposed new remote sensing technique for mesospheric temperature, *Appl. Opt.*, *33*, 7151–7156, doi:10.1364/AO.33.007151.

Gerding, M., M. Alpers, U. von Zahn, R. J. Rollason, and J. M. C. Plane (2000), Atmospheric Ca and Ca^+ layers: Midlatitude observations and modeling, *J. Geophys. Res.*, *105*(A12), 27,131–27,146, doi:10.1029/2000JA900088.

Granier, C., J. P. Jegou, and G. Megie (1985), Resonant lidar detection of Ca and Ca^+ in the upper atmosphere, *Geophys. Res. Lett.*, *12*, 655–658, doi:10.1029/GL012i010p00655.

Granier, C., J. P. Jegou, and G. Megie (1989), Iron atoms and metallic species in the Earth's upper atmosphere, *Geophys. Res. Lett.*, *16*, 243–246, doi:10.1029/GL016i003p00243.

Helmer, M., J. M. C. Plane, J. Qian, and C. S. Gardner (1998), A model of meteoric iron in the upper atmosphere, *J. Geophys. Res.*, *103*(D9), 10,913–10,925, doi:10.1029/97JD03075.

Hunten, D. M. (1967), Spectroscopic studies of the twilight airglow, *Space Sci. Rev.*, *6*, 493–573, doi:10.1007/BF00173704.

Kane, T. J., and C. S. Gardner (1993a), Structure and seasonal variability of the nighttime mesospheric Fe layer at midlatitudes, *J. Geophys. Res.*, *98*(D9), 16,875–16,886, doi:10.1029/93JD01225.

Kane, T. J., and C. S. Gardner (1993b), Lidar observations of the meteoric deposition of mesospheric metals, *Science*, *259*, 1297–1300, doi:10.1126/science.259.5099.1297.

Lübken, F.-J., J. Höffner, T. P. Viehl, B. Kaifler, and R. J. Morris (2011), First measurements of thermal tides in the summer mesopause region at Antarctic latitudes, *Geophys. Res. Lett.*, *38*, L24806, doi:10.1029/2011GL050045.

Ma, Z., and F. Yi (2010), High-altitude sporadic metal atom layers observed with Na and Fe lidars at 30°N, *J. Atmos. Sol. Terr. Phys.*, *72*, 482–491, doi:10.1016/j.jastp.2010.01.005.

Nahar, S. N., M. A. Bautista, and A. K. Pradhan (1997), Electron–ion recombination of neutral iron, *Astrophys. J.*, *479*, 497–503, doi:10.1086/303874.

Plane, J. M. C. (2003), Atmospheric chemistry of meteoric metals, *Chem. Rev.*, *103*(12), 4963–4984, doi:10.1021/cr0205309.

Plane, J. M. C. (2004), A time-resolved model of the mesospheric Na layer: Constraints on the meteor input function, *Atmos. Chem. Phys.*, *4*, 627–638, doi:10.5194/acp-4-627-2004.

Plane, J. M. C., D. E. Self, T. Vondrak, and K. R. I. Woodcock (2003), Laboratory studies and modeling of mesospheric iron chemistry, *Adv. Space Res.*, *32*, 699–708, doi:10.1016/S0273-1177(03)00401-0.

Plane, J. M. C., B. J. Murray, X. Z. Chu, and C. S. Gardner (2004), Removal of meteoric iron on polar mesospheric clouds, *Science*, *304*, 426–428, doi:10.1126/science.1093236.

Raizada, S., and C. A. Tepley (2003), Seasonal variation of mesospheric iron layers at Arecibo: First results from low-latitudes, *Geophys. Res. Lett.*, *30*(2), 1082, doi:10.1029/2002GL016537.

Rodrigo, R., M. J. López-Gonzalez, and J. J. López-Moreno (1991), Variability of the neutral mesospheric and lower thermospheric composition in the diurnal cycle, *Planet. Space Sci.*, *39*, 803–820, doi:10.1016/0032-0633(91)90086-P.

Saunders, R. W., and J. M. C. Plane (2006), A laboratory study of meteor smoke analogues: Composition, optical properties, and growth kinetics, *J. Atmos. Sol. Terr. Phys.*, *68*, 2182–2202, doi:10.1016/j.jastp.2006.09.006.

Self, D. E., and J. M. C. Plane (2002), Absolute photolysis cross-sections for $NaHCO_3$, NaOH, NaO, NaO_2 and NaO_3: Implications for sodium chemistry in the upper mesosphere, *Phys. Chem. Chem. Phys.*, *4*, 16–23, doi:10.1039/b107078a.

Self, D. E., and J. M. C. Plane (2003), A kinetic study of the reactions of iron oxides and hydroxides relevant to the chemistry of iron in the upper mesosphere, *Phys. Chem. Chem. Phys.*, *5*, 1407–1418, doi:10.1039/b211900e.

Slipher, V. M. (1929), Emissions in the spectrum of the light of the night-sky, *Publ. Astron. Soc. Pac.*, *41*, 262–263.

States, R. J., and C. S. Gardner (1999), Structure of the mesospheric Na layer at 40°N latitude: Seasonal and diurnal variations, *J. Geophys. Res.*, *104*(D9), 11,783–11,798, doi:10.1029/1999JD900002.

Stevens, M. H., R. R. Meier, X. Chu, M. T. DeLand, and J. M. C. Plane (2005), Antarctic mesospheric clouds formed from space shuttle exhaust, *Geophys. Res. Lett.*, *32*, L13810, doi:10.1029/2005GL023054.

Tukey, J. W. (1977), *Exploratory Data Analysis*, Addison-Wesley, Reading, Mass.

Vondrak, T., K. R. Woodcock, and J. M. C. Plane (2006), A kinetic study of the reactions of Fe^+ with N_2O, N_2, O_2, CO_2 and H_2O, and the ligand-switching reactions $Fe^+.X + Y \rightarrow Fe^+.Y + X$ ($X = N_2$, O_2, CO_2; $Y = O_2$, H_2O), *Phys. Chem. Chem. Phys.*, *8*, 503–512, doi:10.1039/b508922k.

Wang, Z., X. Chu, W. Huang, W. Fong, J. A. Smith, and B. Roberts (2012), Refurbishment and upgrade of Fe Boltzmann/Rayleigh temperature lidar at Boulder for McMurdo lidar campaign in Antarctica, paper presented at the 26th International Laser Radar Conference, ESA, Porto Heli, Greece, 25–29 June.

Woodcock, K. R. S., T. Vondrak, S. R. Meech, and J. M. C. Plane (2006), A kinetic study of the reactions $FeO^+ + O$, $Fe^+.N_2 + O$, $Fe^+.O_2 + O$ and $FeO^+ + CO$: Implications for sporadic E layers in the upper atmosphere, *Phys. Chem. Chem. Phys.*, *8*, 1812–1821, doi:10.1039/b518155k.

Yi, F., C. Yu, S. Zhang, X. Yue, Y. He, C. Huang, Y. Zhang, and K. Huang (2009), Seasonal variations of the nocturnal mesospheric Na and Fe layers at 30°N, *J. Geophys. Res.*, *114*, D01301, doi:10.1029/2008JD010344.

Zhou, Q., S. Raizada, C. A. Tepley, and J. M. C. Plane (2008), Seasonal and diurnal variation of electron and iron concentrations at the meteor heights above Arecibo, *J. Atmos. Sol. Terr. Phys.*, *70*, 49–60, doi:10.1016/j.jastp.2007.09.012.